energies

MDPI

Article

Optimisation of a Multi-Element Airfoil for a Fixed-Wing Airborne Wind Energy System

Agustí Porta Ko [1,2,†], Sture Smidt [1], Roland Schmehl [2,*] and Manoj Mandru [1]

[1] Kitemill AS, Evangervegen 3, 5704 Voss, Norway; aportako@gmail.com (A.P.K.); ss@kitemill.com (S.S.); mm@kitemill.com (M.M.)
[2] Faculty of Aerospace Engineering, Delft University of Technology, 2629 HS Delft, The Netherlands
* Correspondence: r.schmehl@tudelft.nl
† Current address: CIMNE-Edifici C1 Campus Nord UPC C/Gran Capità s/n, 08034 Barcelona, Spain

Abstract: Airborne wind energy systems benefit from high-lift airfoils to increase power output. This paper proposes an optimisation approach for a multi-element airfoil of a fixed-wing system operated in pumping cycles to drive a drum-generator module on the ground. The approach accounts for the different design objectives of the tethered kite's alternating production and return phases. The airfoil shape is first optimised for the production phase and then adapted for the requirements of the return phase by modifying the flap setting. The optimisation uses the multi-objective genetic algorithm NSGA-II in combination with the fast aerodynamic solver MSES. Once the optimal shape is determined, the aerodynamic performance is verified through CFD RANS simulations with OpenFOAM. The resulting airfoil achieves satisfactory performance for the production and return phases of the pumping cycles, and the CFD verification shows a fairly good agreement in terms of the lift coefficient. However, MSES significantly underpredicts the airfoil drag.

Keywords: airborne wind energy; multi-element airfoil; aerodynamic design; genetic algorithm; optimisation; CFD; MSES; OpenFOAM

Citation: Porta Ko, A.; Smidt, S.; Schmehl, R.; Mandru, M. Optimisation of a Multi-Element Airfoil for a Fixed-Wing Airborne Wind Energy System. *Energies* **2023**, *16*, 3521. https://doi.org/10.3390/en16083521

Academic Editors: Alessandro Bianchini and Davide Astolfi

Received: 28 February 2023
Revised: 13 April 2023
Accepted: 14 April 2023
Published: 18 April 2023

1. Introduction

Wind energy plays an important role in the current transition to renewable energies and is expected to be one of the pillars of future energy systems [1,2]. Airborne wind energy (AWE) is an emerging technology within this sector that promises to reduce both the cost of energy and its environmental impact [3]. Common to AWE systems is the use of tethered flying devices to harness wind energy from altitudes beyond the reach of conventional wind turbines. Several types of tethered flying devices can be distinguished. The most common are fixed-wing and soft kites that use flexible membrane wings steered by a suspended control unit [4].

The conversion of the pulling force of the kite is typically performed using a drum-generator module on the ground. For this purpose, the kite is operated in pumping cycles, alternating between the reel-out and reel-in phases. During the reel-out phase, the kite is flown in crosswind manoeuvres to maximise the tensile power transferred to the ground. During the reel-in phase, the manoeuvres are discontinued and the kite is once again flown at the minimal tether length to start the next cycle. The two phases of the cycle are also denoted as the production and return phases. Maximising the net cycle power while keeping the cost of the system low and ensuring safe operation is a crucial optimisation problem for this technology. The aerodynamic design of the kite has to bridge the distinctly different requirements of the two phases of the cycle. The theory of Loyd [5,6] indicates that the achievable crosswind flight speed depends on the square of the aerodynamic lift-to-drag ratio C_L/C_D of the airborne system, whereas the achievable power is proportional to the C_L^3/C_D^2 ratio. Because the unavoidable contribution of the tether drag sets a lower limit for the combined system drag, the flight speed and tensile power are generally maximised by

maximising the lift of the kite. On the other hand, the reel-in phase should be short and the aerodynamic loading of the kite low to minimise the consumed energy.

An important difference between a crosswind kite and a conventional aircraft is the fact that the loads transferred by the tether are generally significantly higher than the gravitational and inertial loads acting on an untethered aircraft. Consequently, the design requirements for a crosswind kite and a conventional aircraft differ substantially. Considering all the above, multi-element airfoils are well suited for the aerodynamic design of fixed-wing crosswind kites because such airfoils provide higher lift forces and delay stall to higher angles of attack compared to single-element airfoils. This preference is evident in the design choices of the AWE industry, which is reflected in prominent prototypes such as the Makani M600 [7] and the Ampyx Power AP-3 [8], as illustrated in Figures 1 and 2.

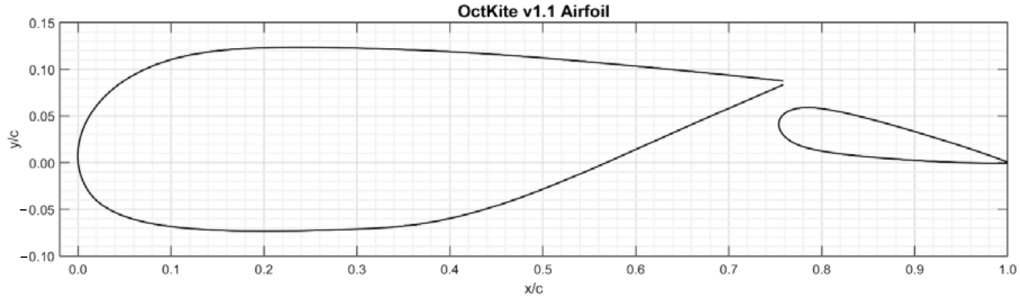

Figure 1. Airfoil of the Makani M600 designed for a nominal power of 600 kW [7].

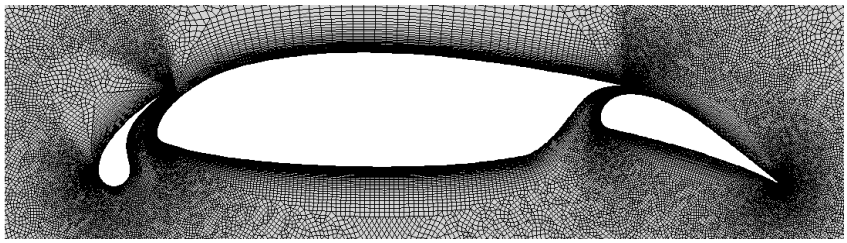

Figure 2. Airfoil of the Ampyx Power AP-3 designed for a nominal power of 150 kW [8].

Table 1 summarises the research on airfoil optimisation for AWE applications found in the scientific literature.

Table 1. Research on the airfoil optimisation and design of AWE systems. RFOIL [9,10] and MSES [11,12] are viscous-inviscid interaction codes for the design and analysis of subsonic airfoils. Adapted from [13].

Reference	Airfoil Type	Optimisation Method	Aerodynamic Solver	Shape Parametrisation
Coenen [14]	Single-skin	Surrogate modelling [15]	RANS	NACA four-digit
Thedens et al. [16]	Ram-air	NSGA II [10]	RFOIL	CST [17]
Kroon [18]	Single-element	NSGA II [10]	RFOIL	CST [17]
Saleem et al. [19]	Single-element	Single-objective GA [19]	XFOIL and RANS verif.	PARSEC [20]
Rangriz et al. [21]	Single-element	NSGA II [10]	XFOIL	IGP [22]
Echeverri et al. [7]	Two-element	Engineering best practices, one parameter at a time	MSES and RANS verif.	-
Drexler [23]	Single- and two-element	CMA-ES [24]	MSES and RANS verif.	Cubic spline interp.
De Fezza et al. [25]	Four-element	One parameter at a time	RANS and MSES verif.	Relative position

Since the present study focuses on multi-element airfoils for fixed-wing AWE systems, only the works of [23,25] and the very recent contribution of [21] on single-element airfoils are included in the following, more detailed discussion.

Drexler [23] optimised the aerodynamic designs of single- and two-element airfoils by applying a widely used technique that was described in [26], which integrates the established two-dimensional airfoil design and analysis tool MSES into the iterative optimisation procedure. MSES solves the Euler equations for the inviscid part of the flow field and uses

a two-equation integral formulation based on dissipation closure for the boundary layers and wake regions. A higher-fidelity but substantially slower RANS solver was used in a postprocessing step to verify the identified optimal design. The objective was to optimise the aerodynamic performance by varying the shape and relative position of the airfoil elements using the covariance matrix adaptation evolution strategy (CMA-ES). However, a return phase was not accounted for in the optimisation since the concept does not operate in pumping cycles but uses onboard ram-air turbines for electricity generation.

De Fezza et al. [25] investigated and further optimised the four-element airfoil for conventional wind turbines, as shown in Figure 3. The optimisation goal was to maximise the ratio C_L^3/C_D^2 by varying certain geometry parameters (scale of flaps, scale of strut, angle of flaps, and vertical distance to strut-main) one at a time while keeping the shape of the individual element airfoils constant. For the aerodynamic analysis, steady-state two-dimensional Reynolds-Averaged Navier-Stokes (RANS) simulations were performed using the open-source CFD solver OpenFOAM. In the absence of experimental data, the simulation approach was verified with MSES. However, the optimisation did not take into account any coupling effects between the four geometry parameters, as each parameter was varied one at a time.

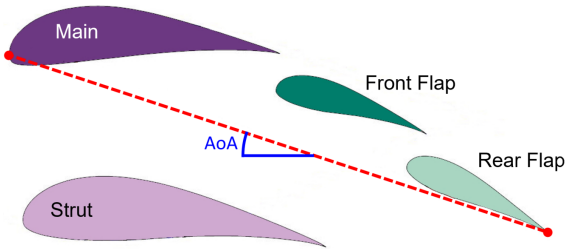

Figure 3. Multi-element airfoil proposed by [27] for a conventional wind turbine.

Rangriz et al. [21] used the improved geometric parameter (IGP) method to create shapes of single-element airfoils within an optimisation process using a genetic algorithm. The resulting airfoils were reminiscent of flapped airfoils, indicating the superiority of a multi-element airfoil design. In this study, only the production phase was accounted for in the optimisation.

Although airfoil optimisation is still relatively new in the emerging AWE sector, it has been widely used for commercial aviation, where multi-element airfoils are required for take-off and landing manoeuvres. Some examples relevant to the present paper are [26,28], where MSES was used in multi- and single-objective genetic algorithms, respectively.

The present paper is based on the graduation project of the first author [13], which was part of the product development of Kitemill AS, one of the leading AWE companies. The aim of the project was to first optimise the design of a multi-element airfoil for a fixed-wing AWE system using MSES and then verify the aerodynamic performance through RANS simulations with OpenFOAM. The developed parametrisation scheme describes the shape and relative position of the element airfoils. The multi-objective genetic algorithm NSGA-II was used to determine the design with the best aerodynamic performance. The specific requirements of the production and return phases were accounted for by using a movable flap.

This paper is structured as follows. Section 2 presents the optimisation methodology, including the definition of the optimisation goal, development of the parametrisation scheme, optimisation algorithm, and aerodynamic solver. Section 3 presents the results, including the optimised airfoil in production- and return-phase configurations, as well as the verification using CFD. Section 4 concludes this study.

2. Methodology

The optimisation procedure illustrated in Figure 4 was presented in [26] and is commonly used for the optimisation of multi-element airfoils.

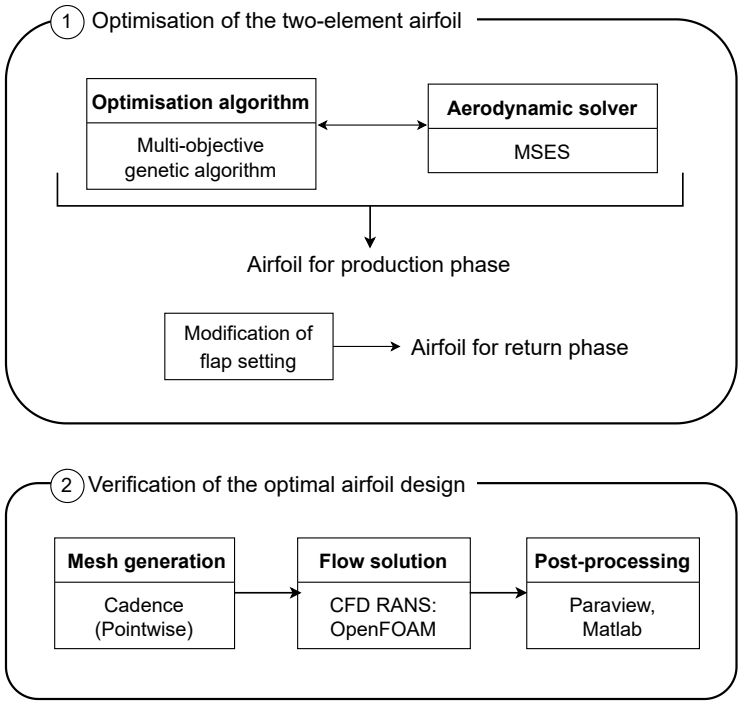

Figure 4. Flowchart of the optimisation procedure. Adapted from [13].

In the first step, which is described in more detail in Section 2.1, a multi-objective genetic algorithm was employed to optimise the multi-element airfoil shape and the flap setting (the relative position of the flap) for the production phases of the pumping cycles. A crucial requirement for a successful optimisation is a suitable description of the full airfoil geometry with a limited set of parameters that provide sufficient flexibility and shape control in the regions of interest. For the present study, the integration of the flap was of particular importance because the flap setting is used to transition from the power to the return phases. Another crucial element for optimisation is the definition of the optimisation goals used to construct the objective functions for the optimisation algorithm. These functions are designed to maximise the generated power in the production phases. The genetic algorithm was implemented in Matlab from where the aerodynamic solver executable was called. The aerodynamic performance of the resulting airfoil was then analysed for the return phase and the flap setting was modified to minimise the lift of the airfoil. Accordingly, the airfoil will have different flap settings for the different phases, leading to an airfoil designed with two different configurations.

In the second step, which is described in more detail in Section 2.2, the aerodynamic performance of the resulting airfoil was verified using higher-fidelity but computationally more expensive CFD simulations. The verification of the airfoil polars was performed for both configurations, the production and return phases.

2.1. Optimisation of the Two-Element Airfoil

This section presents the details of the optimisation procedure, including the optimisation objectives, parametrisation scheme, optimisation algorithm, and aerodynamic solver.

2.1.1. Optimisation Objectives

The optimisation objectives for the production phases of the pumping cycles were closely linked to the implemented control strategy of the AWE system [29], which is

illustrated in Figure 5 as a schematic power curve of the system, together with the two ranges of the set values for the lift coefficient C_L.

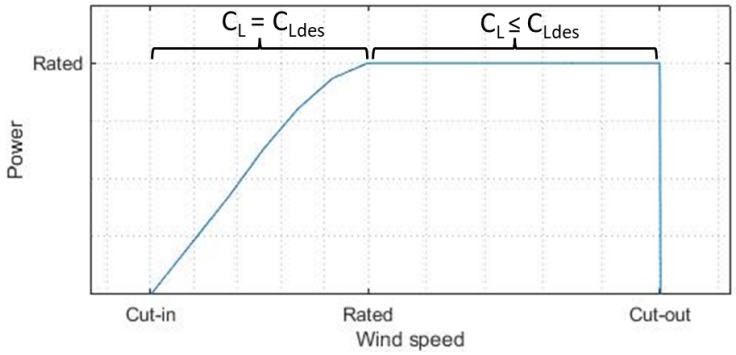

Figure 5. Power curve with set value ranges for the lift coefficient C_L [13].

Below the rated wind speed, a system is operated at the design lift coefficient $C_{L,des}$ of the airfoil. Maximising $C_{L,des}$ also maximises the pulling force of the kite at a specific wind speed. A physical upper limit is the maximum lift coefficient $C_{L,max}$ at which the airfoil begins to stall. To ensure the safe operation of the kite, the present study limited $C_{L,des}$ to 80% of the maximum lift coefficient $C_{L,max}$ and avoided getting anywhere close to this condition. Consequently, the primary optimisation objective was the maximisation of $C_{L,max}$ to maintain a high C_L during operation. Above the rated wind speed, the tether force and generated power can no longer be effectively limited by reeling out faster. In this wind speed regime, the set value of the lift coefficient is decreased to limit the system loads. In the present study, the lift coefficient C_{L2} was lowered to 70% of $C_{L,des}$ and was considered representative of the operation above rated wind speed.

A secondary optimisation objective was to maximise the ratio C_L^3/C_D^2 for both wind speed ranges. Therefore, the three objective functions for the production phase can be formulated as

$$f_1(X) = C_{L,max}, \tag{1}$$

$$f_2(X) = \left.\frac{C_L^3}{C_D^2}\right|_{C_{L,des}}, \tag{2}$$

$$f_3(X) = \left.\frac{C_L^3}{C_D^2}\right|_{C_{L2}}, \tag{3}$$

where $X = x_1, x_2, x_3, \ldots, x_n$ is a set of design variables that fully defines the geometry of the airfoil, as described in Section 2.1.2.

The return-phase airfoil configuration aims to reach a low C_L such that the tether force is as low as possible and the consumed power is minimised. Such an objective is accounted for by modifying the flap setting during the return phase.

2.1.2. Parametrisation Scheme

The purpose of the parametrisation scheme is to fully define the geometry of the multi-element airfoil using a set X of n scalar variables. Two types of design variables are distinguished: airfoil shape and flap-setting variables.

For efficient use in an optimisation procedure, the number of design variables should be as low as possible and the scheme should be flexible enough to allow for good shape control. A high degree of flexibility is favourable for the main element since the aerodynamic performance is particularly sensitive to the slot shape, which is affected by the main element's geometry at the trailing edge. Therefore, the simple NACA four-digit nomenclature was combined with a parameterised modification along the trailing edge. In the present

work, this modification is referred to as a 'cut' and is defined by a 3rd-order polynomial, requiring three additional design variables: the starting location along the lower surface of the main element, the ending location along the upper surface of the main element, and the curvature of the cut. In this way, the number of shape-related design variables of the main element is kept relatively low and the design flexibility matches the specific problem of finding a suitable flap integration. The shape of the flap has a relevant effect on the overall performance but the NACA method is deemed flexible enough to define it. A key reason for selecting the NACA nomenclature for the flap and as a 'backbone' for the main element was that the thickness becomes straightforward to control. This is relevant because the airfoil thickness is determined mainly by the structural requirements and should thus be easily constrained in the optimisation procedure.

The relative position between the flap and the main element, denoted here as the flap setting, is defined by the flap overlap, gap, chord, and deflection. The gap is defined as the vertical distance between the main element's trailing edge and the flap, whereas the overlap is the horizontal distance. The parametrisation requires a total of 12 design variables, as illustrated in Figures 6 and 7 and listed in Table 2. It should be noted that the main element thickness is not a design variable since it is given as a constraint. This constraint comes from the wing structural design since the thickness of the airfoil determines the thickness of the wing's main spar.

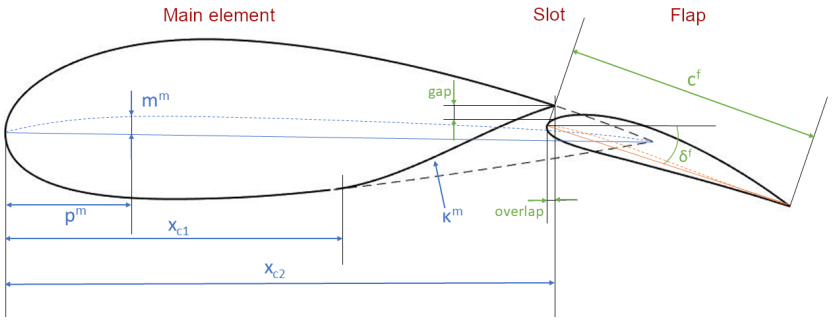

Figure 6. Design variables that define the shape of the main element (blue) and the flap setting (green) [13].

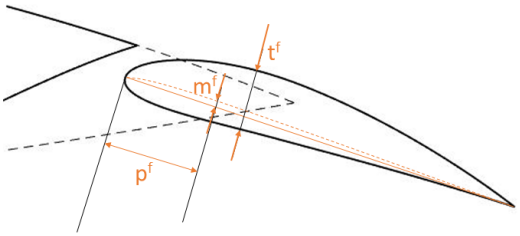

Figure 7. Design variables that define the flap shape [13].

Table 2. List of shape and setting design variables [13].

Main Element Shape	Flap Shape	Flap Setting
Camber, m^m	Flap camber, m^f	Flap gap
Position max. camber, p^m	Position max. camber, p^f	Overlap
Cut starting position, x_{c1}	Flap thickness, t^f	Flap deflection, δ^f
Cut ending position, x_{c2}		Flap chord, c^f
Cut curvature, κ^m		

2.1.3. Genetic Algorithm

A genetic algorithm is a stochastic metaheuristic optimisation technique inspired by the process of natural selection belonging to the larger class of evolutionary algorithms [30,31].

The working principle is based on a population of individuals, here airfoils, with their fitness quantified by one or more objective functions. The optimisation goal can be to maximise or minimise the values of the objective functions. As part of the selection process, the fitter individuals produce the next generation of airfoils through genetic operators, as illustrated in Figure 8. Crossover is used to combine the genetic information of two parents to generate new offspring, whereas mutation is used to maintain the genetic diversity of the chromosomes in a population by randomly changing a property of an individual. Elitist selection automatically passes the best individuals to the next generation. This process of selection and variation is repeated until the algorithm meets the convergence criteria, which, in this case, is when the objective functions no longer improve.

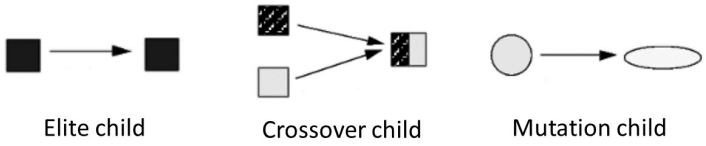

Figure 8. Variation methods of a genetic algorithm. Adapted from [32].

Although a genetic algorithm is computationally expensive due to its population-based nature, it was selected over conventional gradient-based methods for its capability of dealing with multiple objectives in a very flexible manner (Pareto front) and its robustness in finding the global optima even in highly non-linear design spaces. For the present study, the Non-Dominated Sorting Genetic Algorithm II (NSGA-II) [33,34] was used. The algorithm is an extension of the general GA concept that aims to optimise multiple objective functions. Implementation in Matlab is provided through the use of the function *gamultiobj* [35], which allows for the easy control of the GA operators, including crossover and mutation. The population size was set to 20 individuals and the number of computed generations depended on the iterations needed to meet the convergence criteria.

2.1.4. Aerodynamic Solver

The optimisation procedure uses the two-dimensional aerodynamic solver MSES to evaluate the load distribution on a specific multi-element airfoil [11,12]. MSES is a viscous-inviscid interaction code that combines a finite-volume solver for the Euler equations in the inviscid part of the flow field with an integral formulation of the boundary layers and wake regions [36]. The finite-volume mesh is generated automatically by intersecting the inviscid flow streamlines and splines emitting orthogonally from the airfoil surface, where the inviscid flow streamlines are precomputed using a panel method. This procedure results in a high-quality structured mesh since it attains satisfactory orthogonality. Moreover, the mesh parameters are user-defined so they can be tuned to reach a smooth grid with minimal skewness, and the cells' aspect ratio is not too high. MSES was selected for the following reasons:

- the automatically generated mesh (see Figure 9) was of good quality and adapted well to variations of the geometry;
- the computation time was short;
- the executable ran without a graphical user interface and with input and output via text files, that is, it can be operated using scripts and can be easily combined with the genetic algorithm in Matlab;
- the software is open source and can be used for academic purposes;
- the solver produced fairly accurate results for the linear region of C_L and $C_{L,max}$, although there were larger errors for the C_D [28,37,38].

A drawback of using MSES is that the solver does not always converge, which can be related to the occurrence of large flow-separation regions as a result of specific flow conditions, complex geometry, or a combination of both. Since convergence problems are undesirable in an automated optimisation process, the issue was mitigated by adjusting the bounds of

the design variables and finding mesh parameters that could produce a high-quality mesh for a wide range of geometries. Moreover, a human-in-the-loop approach was employed by manually monitoring and controlling the optimisation algorithm to ensure that all aerodynamic analyses converged.

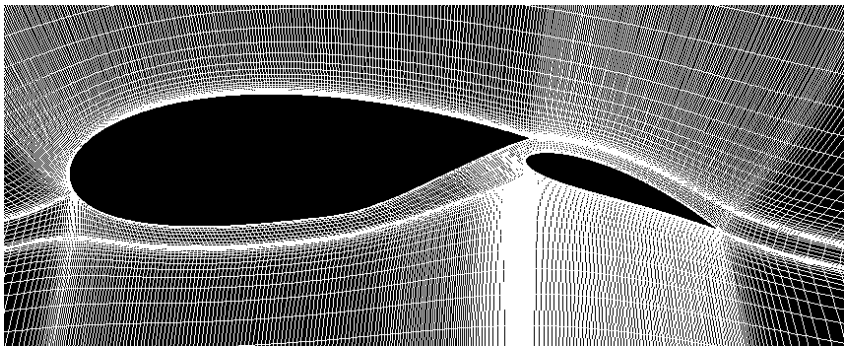

Figure 9. Automatically generated mesh from the multi-element airfoil geometry [13].

2.1.5. Flow Conditions

The optimisation was run under specific flow conditions representative of the conditions experienced by the kite during operation. The relevant flow conditions to be determined were the Reynolds number and the boundary layer type (laminar or turbulent). The representative flow speed for the kite system operation was v_{ref} = 45 m/s. Although the kite can operate at a wide range of speeds, a reference value needed to be chosen for this design phase. The density ρ and dynamic viscosity μ were taken at a reference temperature of 15°, leading to the values $\rho = 1.225$ kg/m^3 and $\mu = 1.81 \times 10^{-5}$ kg/(ms). The reference length, which was provided by the company, was representative of the whole wing. Since the wing has varying chords in the spanwise direction, an estimation of the mean aerodynamic chord (MAC) was utilised, which was assumed to be close to a length of $l = 1$ m. By substituting in the Reynolds number equation, we obtain

$$\mathrm{Re} = \frac{v\rho l}{\mu} \approx 3 \times 10^6 \tag{4}$$

which was utilised for the whole optimisation procedure for both the MSES and RANS simulations. From the company's perspective, the leading edge of the kite wing would become dirty after a certain period of time and would remain so during prolonged operation. Deposits on the wing's LE can trigger turbulent flow in the boundary layer. Therefore, a fully turbulent boundary layer was used for the airfoil optimisation, even though it might partially remain laminar during periods of operation when the LE is clean. This approach is considered conservative since a turbulent boundary layer is known to increase the viscous drag on the airfoil's surface [39].

2.2. Verification of the Optimal Airfoil Design

Once the optimal design of the multi-element airfoil was identified, its aerodynamic performance was verified through RANS simulations. The workflow of the higher-fidelity toolchain is illustrated in the bottom part of Figure 4 as progressing from mesh generation to flow solution and eventually post-processing.

2.2.1. Setup of RANS Simulations

The finite-volume mesh was generated using the commercial meshing software Cadence, formerly known as Pointwise. The software can be used with its own scripting language Glyph to efficiently construct high-quality meshes of parametrised geometries. Figure 10 shows the topology of the generated hybrid mesh structured around the airfoil and in the wake and unstructured otherwise. The body-fitted O-grid mesh was generated

through hyperbolic extrusion such that the first cell layer is orthogonal around the surface of both elements, as shown in Figure 11.

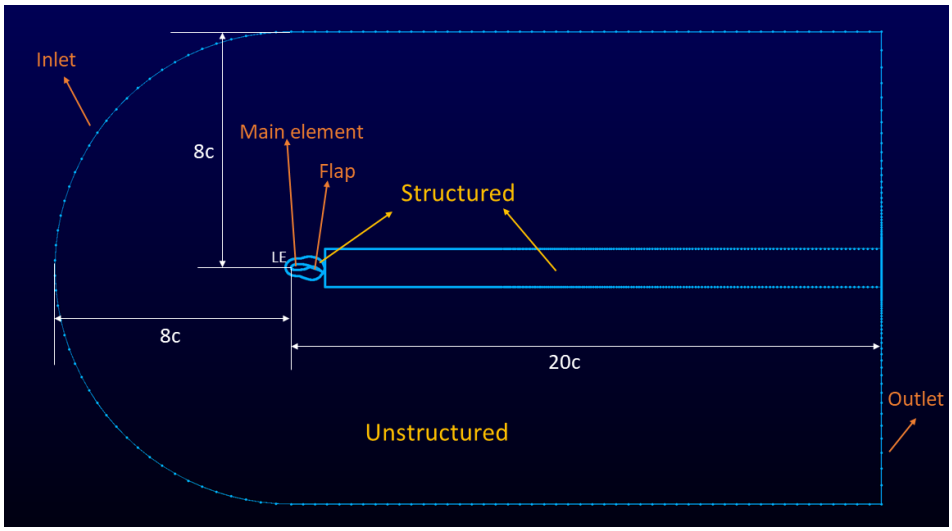

Figure 10. Topology of the hybrid mesh [13].

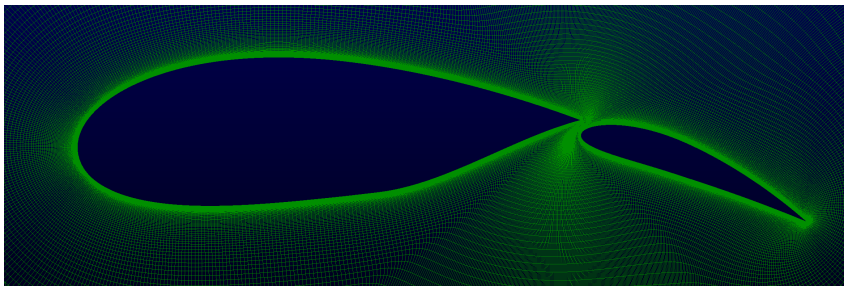

Figure 11. Structured hyperbolic mesh close to the airfoil surface [13].

This approach allowed us to easily adjust the non-dimensional height y^+ of the first cell layer, which was determined through a mesh sensitivity analysis, by progressively decreasing the value of y^+ to investigate the effect on the aerodynamic coefficients C_L and C_D. The baseline case employed for such a procedure is a NACA 2424 airfoil at $\alpha = 5°$. With the reduction of y^+, the length of the cells along the surface was decreased to maintain the cell aspect ratio within reasonable bounds. The mesh sensitivity of the computed aerodynamic coefficients is shown in Figure 12 and Table 3.

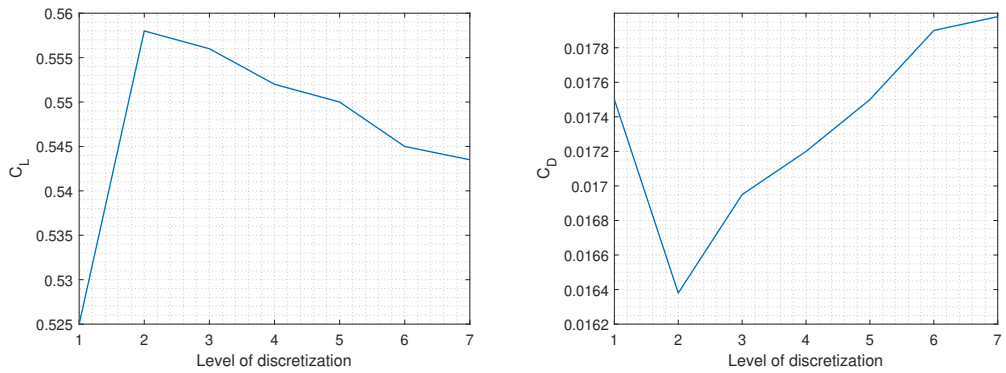

Figure 12. Sensitivity of computed aerodynamic coefficients to the mesh resolution, for a NACA 2424 airfoil at $\alpha = 5°$ [13].

Figure 12 shows that the mesh sensitivity of the aerodynamic coefficients weakens for values of y^+ below 0.23. Notice that the relative variation of the lift coefficient above the second level of refinement, i.e., below $y^+ = 23$, is less than 3%. On the other hand, the drag coefficient varies significantly in that same range, with a variation close to 9%, indicating that it is preferable to employ a small y^+ of around 0.2 to reduce the effect of the mesh resolution.

Table 3. Mesh properties and aerodynamic coefficients for the different levels of discretisation, for a NACA 2424 airfoil at $\alpha = 5°$ [13].

Level of Discretisation	Height of First Cell	y^+	C_L	C_D
1	2×10^{-3}	230	0.525	0.0175
2	2×10^{-4}	23	0.558	0.0164
3	2×10^{-5}	2.29	0.556	0.0169
4	1×10^{-5}	1.15	0.552	0.0172
5	5×10^{-6}	0.57	0.550	0.0175
6	2×10^{-6}	0.23	0.545	0.0179
7	1×10^{-6}	0.11	0.544	0.0180

Following the generation of the mesh, the flow field was computed using the open source software OpenFOAM with the steady-state solver SimpleFoam for the incompressible turbulent flow. The k-ω SST turbulence model [40] was used to close the RANS equations because of its superior performance for both external flows and boundary layers. The model employs two additional transport equations, one for the turbulence kinetic energy k and one for the specific turbulence dissipation rate ω. It cannot model the transition from laminar to turbulent flow and, consequently, assumes that the boundary layer is fully turbulent, which adapts well to our problem, as stated in Section 2.1.5. This specific combination of physical models was recommended by [19,26] for the aerodynamic analysis of conventional airfoils and by [41] for the analysis of a leading-edge inflatable kite airfoil.

The numerical scheme used for the time derivative terms was a second-order implicit (backwards), whereas the gradient and divergence terms were computed through the linear interpolation of values from cell centres to face centres (Gauss linear).

The CFD results were post-processed using the open source software Paraview, mainly to illustrate and investigate the flowfield around the airfoil. Convergence plots or the surface pressure distribution along the airfoil were computed using Matlab scripts.

2.2.2. RANS Simulation Validation

Before verifying the computed MSES polars with OpenFOAM, the CFD solver was validated with a simple test case to quantify its accuracy with respect to the experimental data. The simulation case for this validation was an NACA 2424 at $\mathrm{Re} = 2.9 \times 10^6$, where the experimental polars were obtained from [42]. The comparison of the computed and measured data is shown in Figure 13, including the simulation results obtained using the $k - \omega$ SST and $k - \varepsilon$ turbulence models.

The comparison shows that the $k - \omega$ SST turbulence model performs significantly better, accurately predicting the lift coefficient in the linear region and capturing also fairly well the stall region, while only slightly overpredicting the maximum lift. The model clearly overestimates the drag but still stays rather close to the experimental data, roughly within 13% of relative error. The $k - \varepsilon$ turbulence model is also accurate in terms of lift in the linear region but is not capable of capturing the flow separation in the stall region, and drag is significantly overpredicted for the entire C_L range.

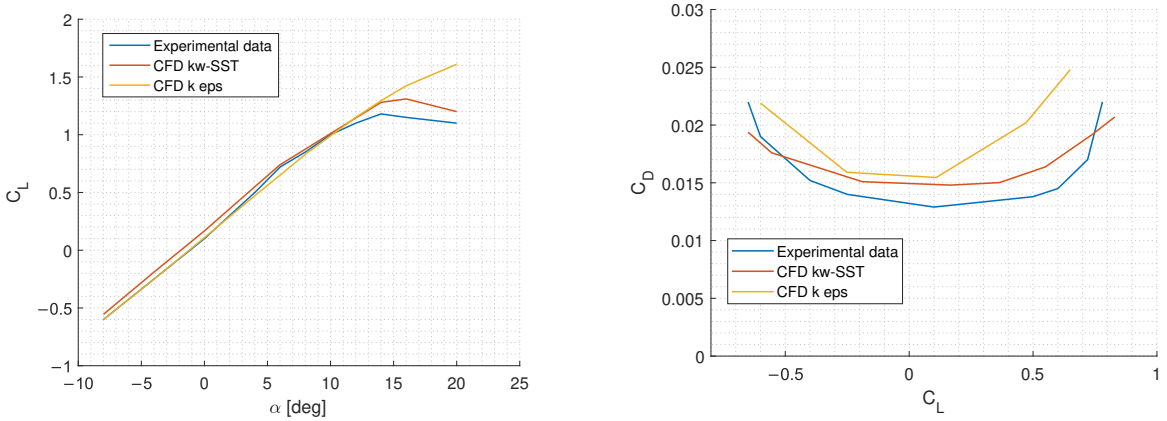

Figure 13. Using experimental data for a NACA 2424 airfoil from [42] to validate the CFD setup [13].

3. Results and Discussion

The presentation of the results follows the structure of Section 2, first discussing the optimisation results and then discussing the verification of the identified optimal airfoil.

3.1. Optimisation Results

The optimisation results are presented separately for the production and return phases.

3.1.1. Production Phase

The result of the multi-objective optimisation was a Pareto front, which was represented by the set of airfoils that could not improve one objective function without having a detrimental effect on the others. As we used three objective functions, the Pareto front was actually a surface in a three-dimensional space. From this surface, we selected an airfoil in such a way that the $C_{L,max}$ was given a relatively high weight. The geometry of this specific airfoil and its aerodynamic performance are illustrated in Figures 14 and 15, respectively.

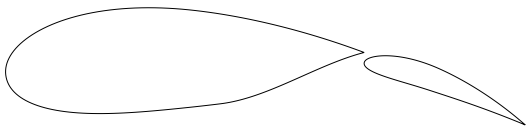

Figure 14. Selected airfoil for the production phase [13].

The polars indicate a maximum lift coefficient of $C_{L,max} = 2.95$, which leads to a design lift coefficient of $C_{L,des} = 2.36$. There is an AoA margin of about $\Delta\alpha = 7.5^o$ between these two values, which is considered sufficient to prevent the kite from operating close to stall. The AoA margin of $\Delta\alpha = 5^o$ given in [7] for Makani's M600 supports this assessment. It should be noted that the airfoil's $C_{L,des}$ differs from the wing's $C_{L,des}$ because of the neglected three-dimensional effects and from the kite's $C_{L,des}$ due to neglected lift contributions from the tail and fuselage. The ratio of C_L^3/C_D^2 is highest close to $C_{L,des}$, indicating that the kite will operate efficiently when using $C_{L,des}$ below the rated wind speed. For higher wind speeds, the C_L will have to be reduced to cap the tether force or generated power, resulting in a lower C_L^3/C_D^2 ratio. The pitching moment coefficient is approximately $C_m = -0.31$, which can be balanced with the kite's elevator.

3.1.2. Return Phase

As shown in Figure 15, the airfoil optimised for the production phase reaches a $C_{L,min} \approx 0.5$ at $\alpha = -10^o$. This lift coefficient is not low enough for an efficient return phase. Moreover, there should be a certain margin between the C_L employed in the return phase

and the $C_{L,min}$. This is achieved by rotating the flap upwards, as shown in Figure 16. The effect of the adjusted flap setting is a downward shift of the C_L-α curve.

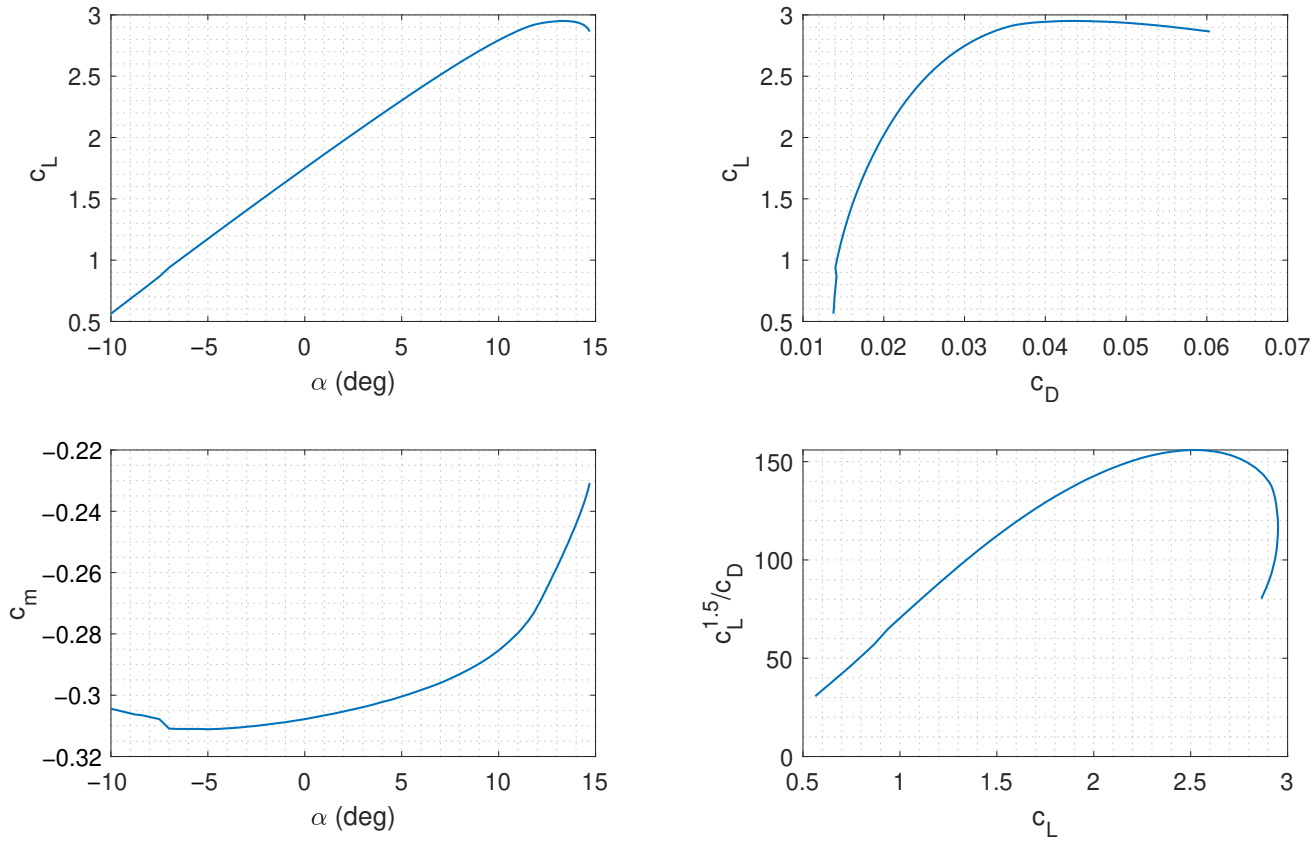

Figure 15. Polars of the selected airfoil for the production phase [13]. To limit the range of numerical values, the square root of the C_L^3/C_D^2 ratio is plotted.

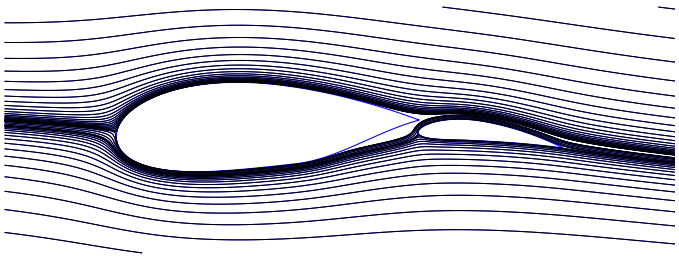

Figure 16. Streamlines around the airfoil with the flap rotated upwards at $\alpha = -4^o$, and visible flow separation on the pressure side of the main element's trailing edge [13].

We observed that the flow phenomenon constraining $C_{L,min}$ was the flow separation at the lower surface of the main element's trailing edge, which is clearly visible in Figure 16. To mitigate this, the high-speed flow induced by the flap can be used to re-energise the main element's boundary layer at the point of flow separation. To achieve this, the flap must have a certain overlap with the main element; therefore, the flap should be both translated and rotated. These two geometrical operations can be achieved by a single rotation around a hinge point outside the flap. The various pivot points (PP) that we evaluated are shown in Figure 17, together with their respective rotated flaps.

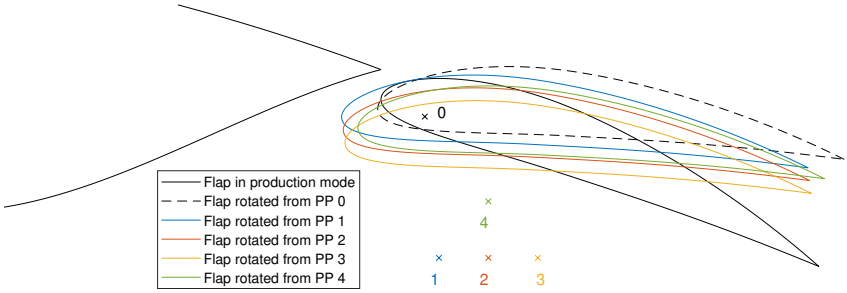

Figure 17. Close-up view of the flap rotated upwards for the return phase from the various pivot points [13].

The mentioned effect of the high-speed flow induced by the flap to mitigate flow separation can be seen in Figure 18, where the formerly separated flow now stays attached at the same angle of attack.

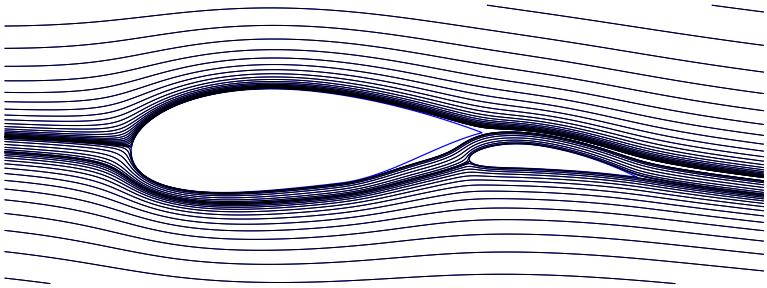

Figure 18. Streamlines around the airfoil with the flap rotated upwards from PP 3 at $\alpha = -4°$ and visible mitigation of the flow separation [13].

As a consequence of this effect, each flap setting results in a different aerodynamic performance. The $C_{L,min}$ is now the parameter of interest, as shown in Figure 19. As anticipated, lower C_L values were obtained when increasing the overlap, and it was also observed that a specific gap was useful for reducing the $C_{L,min}$.

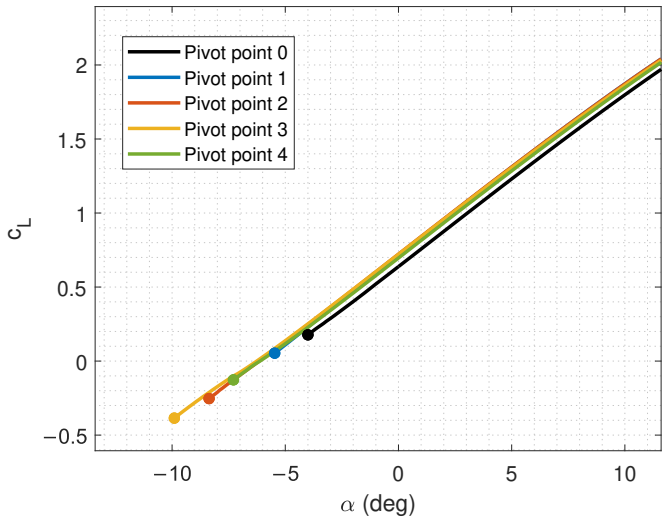

Figure 19. C_L-α polar of the airfoil with the flap rotated from the various pivot points [13].

From an aerodynamic point of view, a hinge point outside the flap is undesirable due to the drag penalty of the required mechanical system. However, the solution was considered acceptable given the benefits that could be achieved by meeting the design goal

for the return phase. We identified pivot point 4 as the most suitable option in terms of the obtained $C_{L,min} = -0.1$ and proximity to the flap, which are useful from both aerodynamic and mechanical perspectives.

3.2. CFD Verification

The lift and drag polars of the airfoil optimised for the production and return phases were used for the verification of the aerodynamic performance. Figure 20 shows the polars for the production phase airfoil with the flap down. The lift curves are almost on top of each other, differing only by a small offset. The coefficients predicted by CFD were slightly lower across the entire range of the angle of attack. MSES captured the maximum lift coefficient well, with a small shift to lower angles. The slight overprediction of the lift coefficient in the linear region was also found in [28] and was attributed to the inaccuracies in computing the gap flow between the main element and the flap. A good agreement in $C_{L,max}$ was also obtained in this reference. MSES significantly underpredicted the drag coefficient, with the discrepancies more pronounced at higher angles of attack. The underprediction of the aerodynamic drag was anticipated because other authors [7,23,25,28,37,43] observed similar behaviour when comparing against the results of RANS solvers.

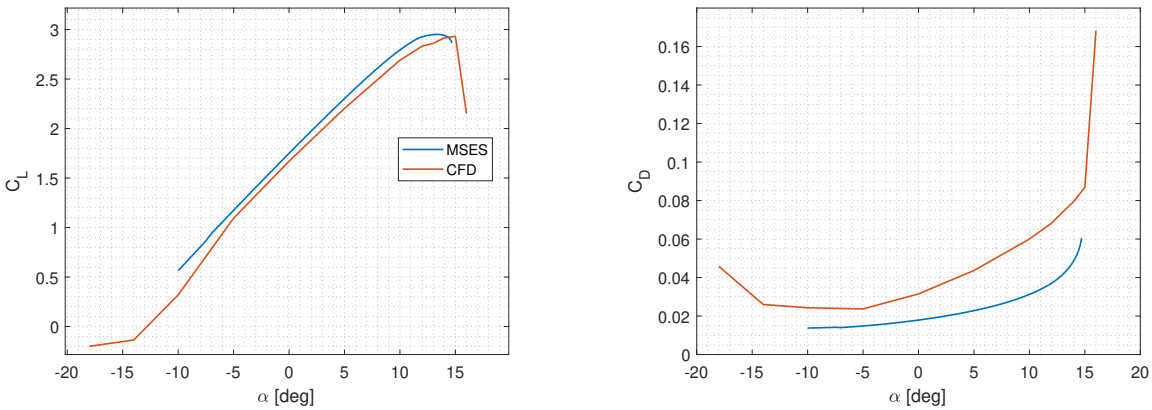

Figure 20. Verification of the lift and drag polars for the airfoil optimised for the production phase with the flap down [13].

The verification of the lift and drag polars of the airfoil optimised for the return phase with the flap up led to similar conclusions. As shown in Figure 21, the maximum lift coefficient was again well-captured by MSES, with a similar small shift to lower angles. The drag polars showed a similar trend to the polars computed for the production-phase airfoil, only now the two polar curves were slightly closer.

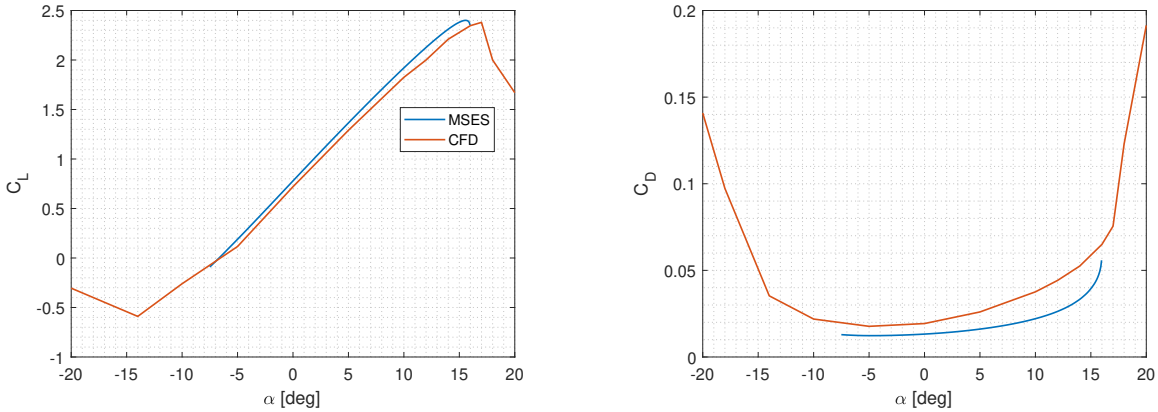

Figure 21. Verification of the lift and drag polars for the airfoil optimised for the return phase with the flap up [13].

The mitigating effect of the flap setting on flow separation in the gap flow was also investigated through CFD simulations. The flow fields depicted in Figure 22 support the MSES results and clearly show the effect of the designed flap setting compared to the initial flap setting.

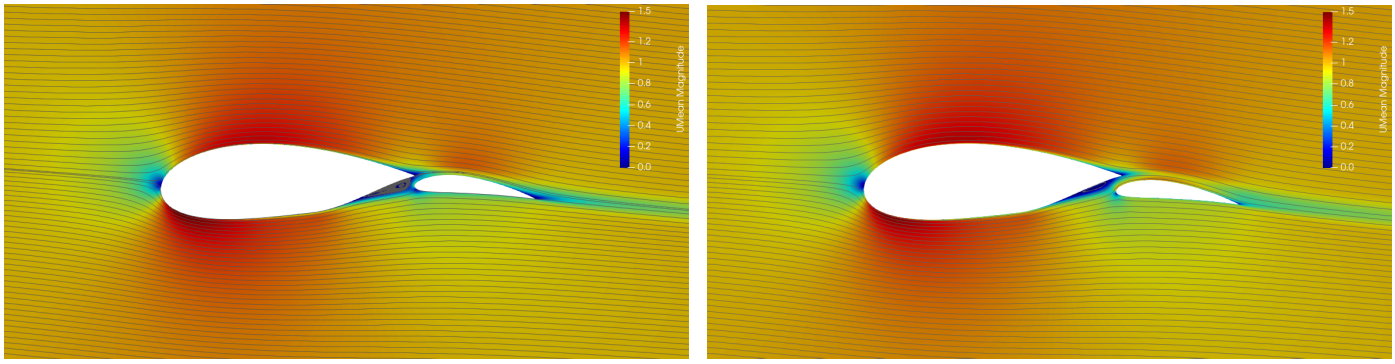

Figure 22. Visualisations of the CFD simulations using streamlines and contour plots of the mean velocity magnitude at an angle of attack of $\alpha = -4^{\circ}$. The velocity magnitude is non-dimensionalised with the freestream velocity $v_{ref} = 45$ m/s. Left: initial flap setting for the return phase with the hinge point inside the flap and visible flow separation. Right: designed flap setting for the return phase with the hinge point outside the flap and mitigated flow separation [13].

4. Conclusions

This paper describes an optimisation approach for a two-element airfoil of a fixed-wing airborne wind energy system that is operated by pumping cycles. The production and return phases of the cycles have distinctly different design requirements. To account for this, the airfoil geometry is first optimised for the production phases, followed by an adjustment of the flap setting to ensure its efficient performance in the return phases. The aerodynamic performance of the resulting airfoil was verified by comparing the computed lift and drag polars with higher-fidelity RANS simulations.

The developed parametrisation scheme provides flexible shape control with a limited set of design variables. The scheme combines the NACA four-digit nomenclature for both elements with a modification of the main element's trailing edge geometry to enhance the integration of the flap and control the shape of the slot. Moreover, the scheme facilitates the constraining of the thickness of the elements, which is required for structural reasons.

The multi-objective genetic algorithm NSGA-II proved to be robust and efficient in finding the global optima in the highly non-linear design space and providing a Pareto front to make tradeoffs for choosing an optimal airfoil design. The gradient-free optimisation method was able to cope with missing sensitivity information in regions of the design space caused by occasional convergence problems of the aerodynamic solver MSES. Although it was possible to avoid such convergence problems in many cases by carefully adjusting the mesh parameters, complete elimination was not possible. The unfavourable effect of unconverged MSES runs was mitigated by employing a human-in-the-loop technique, with the designer monitoring and analysing the problematic cases so that the optimisation algorithm could continue. However, MSES was selected as an aerodynamic solver for the optimisation because of its low computational cost, fairly accurate results, and ease of integration with an optimisation algorithm. Furthermore, MSES can automatically generate a hyperbolic mesh of high quality, which is particularly useful for complex multi-element airfoil geometries.

To maximise the power output of the production phase, three objective functions were prioritised. The highest-priority objective was the maximisation of the operational C_L, whereas the maximisations of the C_L^3/C_D^2 ratio for wind speeds below and above the rated wind speed were of secondary importance. The lift and drag polars indicated a satisfactory performance of the optimised airfoil in the production phase. For the return phase, the lift coefficient of the airfoil was minimised by rotating the flap upwards around

a specific pivot point so that the flap-up configuration had a certain overlap with the main element. This specific geometric feature induced a high-velocity flow that re-energised the boundary layer on the main element and mitigated flow separation. Practically, the overlap can be created by placing the pivot point outside the flap so that the flap is rotated and translated at the same time. The optimisation resulted in a two-element airfoil with satisfactory performance for both the reel-out and reel-in phases achieved using a movable flap. Such a mechanism is crucial for the development of AWE systems so that the entire operational cycle can be efficiently performed.

The CFD setup was first validated using the experimental data of a single-element airfoil, NACA 2424, which showed fairly good agreement. The $k-\omega$ SST turbulence model was selected because of its superior performance in dealing with both external and boundary layer flows. The verification results showed good agreement for the lift coefficient both in the linear region and for $C_{L,max}$. On the other hand, the drag coefficient was significantly underpredicted by MSES. The flow separation phenomena in the return phase were also investigated through CFD simulations. The performance improvement achieved by varying the location of the flap pivot point based on MSES analyses is supported by the flow field visualisations obtained from CFD.

Regarding recommendations for future work, several areas could be extended. This work studied two-element airfoils to meet the high-lift requirements of an AWE system. However, it may be worth investigating three-element airfoils to evaluate the trade-off between the added complexity and aerodynamic improvement. Furthermore, adding validation with a multi-element airfoil would help to determine whether the agreement with the experimental data varies with the addition of an element. Finally, conducting an experimental simulation on the optimised airfoil would be highly beneficial in assessing the accuracy of the solvers used in this study.

Author Contributions: Conceptualisation, A.P.K., S.S., R.S. and M.M.; methodology, A.P.K., S.S., R.S. and M.M.; software, A.P.K.; validation, A.P.K.; writing—original draft preparation, A.P.K.; writing—review and editing, S.S. and R.S.; supervision, S.S., R.S. and M.M. All authors have read and agreed to the published version of the manuscript.

Funding: This research was funded by The European Union's Horizon 2020 SME Phase 2 project AWE with grant number 881193. The APC was funded by the Delft University of Technology.

Data Availability Statement: Not applicable.

Acknowledgments: A.P.K. would like to thank Kitemill AS for providing the opportunity to contribute to this AWE system design project. Furthermore, A.P.K would like to thank Aerotrope Ltd for their valuable advice regarding the CFD setup and validation.

Conflicts of Interest: The authors declare no conflict of interest.

Abbreviations

The following abbreviations are used in this manuscript:

AoA	Angle of attack
AWE	Airborne wind energy
CFD	Computational fluid dynamics
CMA-ES	Covariance matrix adaptation evolution strategy
CST	Class shape transform
GA	Genetic algorithm
IGP	Improved geometric parameter
NACA	National Advisory Committee for Aeronautics
NSGA II	Non-Dominated Sorting Genetic Algorithm II
PARSEC	Parametric sectioning
PP	Pivot point
RANS	Reynolds-Averaged Navier-Stokes

References

1. IRENA. *Future of Wind—Deployment, Investment, Technology, grid Integration and Socio-Economic Aspects (A Global Energy Transformation Paper)*; Technical report; International Renewable Energy Agency: Abu Dhabi, United Arab Emirates, 2019.
2. IRENA. *Global Energy Transformation: A Roadmap to 2050*, 2019th ed.; Technical report; International Renewable Energy Agency: Abu Dhabi, United Arab Emirates, 2019.
3. IRENA. *Offshore Renewables: An Action Agenda for Deployment*; Technical report; International Renewable Energy Agency: Abu Dhabi, United Arab Emirates, 2021.
4. Cherubini, A.; Papini, A.; Vertechy, R.; Fontana, M. Airborne Wind Energy Systems: A review of the technologies. *Renew. Sustain. Energy Rev.* **2015**, *51*, 1461–1476. [CrossRef]
5. Loyd, M.L. Crosswind kite power. *J. Energy* **1980**, *4*, 106–111. [CrossRef]
6. Vermillion, C.; Cobb, M.; Fagiano, L.; Leuthold, R.; Diehl, M.; Smith, R.S.; Wood, T.A.; Rapp, S.; Schmehl, R.; Olinger, D.; et al. Electricity in the Air: Insights From Two Decades of Advanced Control Research and Experimental Flight Testing of Airborne Wind Energy Systems. *Annu. Rev. Control* **2021**, *52*, 330–357. [CrossRef]
7. Echeverri, P.; Fricke, T.; Homsy, G.; Tucker, N. *The Energy Kite-Selected Results from the Design, Development and Testing of Makani's Airborne Wind Turbines-Part 1*; Technical report; Makani Power: Alameda, CA, USA, 2020. Available online: https://archive.org/details/theenergykite (accessed on 10 October 2022) .
8. Vimalakanthan, K.; Caboni, M.; Schepers, J.; Pechenik, E.; Williams, P. Aerodynamic analysis of Ampyx's airborne wind energy system. *J. Phys. Conf. Ser.* **2018**, *1037*, 062008. [CrossRef]
9. Van Rooij, R.P.J.O.M. *Modification of the Boundary Layer Calculation in RFOIL for Improved Airfoil Stall Prediction*; Technical Report IW-96087R; Delft University of Technology: Delft, The Netherlands, 1996.
10. De Oliveira, G. Wind Turbine Airfoils with Boundary Layer Suction. Master's Thesis, Delft University of Technology, Delft, The Netherlands, 2011. Available online: http://resolver.tudelft.nl/uuid:c7bad1bd-b268-4dda-b50e-0989b6261d3c (accessed on 10 October 2022).
11. Drela, M. *MSES Multi-Element Airfoil Design/Analysis Software–Summary*; Technical report; Massachusetts Institute of Technology: Cambridge, MA, USA, 1994.
12. Drela, M. A User ' s Guide to MSES 3.05. Available online: https://web.mit.edu/drela/Public/web/mses/mses.pdf (accessed on 31 Jaunary 2023).
13. Porta i Ko, A. Optimization of a Multi-Element Airfoil for a Rigid Airborne Wind Energy Kite. Master's Thesis, Delft University of Technology, Delft, The Netherlands, 2022. Available online: http://resolver.tudelft.nl/uuid:607bab45-4d6c-4308-8f16-84f332fe3f6b (accessed on 1 March 2023).
14. Coenen, R. Single Skin Kite Airfoil Optimization for Airborne Wind Energy Systems. Master's Thesis, Delft University of Technology, Delft, The Netherlands, 2018. Available online: http://resolver.tudelft.nl/uuid:fdcf8423-11f0-4b33-956e-3e761635ac41 (accessed on 10 October 2022).
15. Gorissen, D.; Couckuyt, I.; Demeester, P.; Dhaene, T.; Crombecq, K. A Surrogate Modeling and Adaptive Sampling Toolbox for Computer Based Design. *J. Mach. Learn. Res.* **2010**, *11*, 2051–2055. Available online: http://jmlr.org/papers/v11/gorissen10a.html (accessed on 15 October 2022).
16. Thedens, P.; de Oliveira, G.; Schmehl, R. Ram-air kite airfoil and reinforcements optimization for airborne wind energy applications. *Wind Energy* **2019**, *22*, 653–665. [CrossRef]
17. Kulfan, B.M. Recent extensions and applications of the 'CST' universal parametric geometry representation method. *Aeronaut. J.* **2010**, *114*, 157–176. [CrossRef]
18. Kroon, E.J. Airborne Wind Energy Airfoils: Design of Pareto-Optimal Airfoils for Rigid Wing Systems in the Field of Airborne Wind Energy. Master's Thesis, Delft University of Technology, Delft, The Netherlands, 2018. Available online: http://resolver.tudelft.nl/uuid:dd976c1b-edda-4941-8b28-c28f87284a77 (accessed on 3 October 2022).
19. Saleem, A.; Kim, M.H. Aerodynamic performance optimization of an airfoil-based airborne wind turbine using genetic algorithm. *Energy* **2020**, *203*, 117841. [CrossRef]
20. Sobieczky, H. Parametric Airfoils and Wings. In *Recent Development of Aerodynamic Design Methodologies: Inverse Design and Optimization*; Fujii, K., Dulikravich, G.S., Eds.; Vieweg+Teubner Verlag: Wiesbaden, Germany, 1999; pp. 71–87. [CrossRef]
21. Rangriz, S.; Kheiri, M. Design of optimal airfoils for airborne wind energy applications. AIAA 2023-1155. In Proceedings of the AIAA SCITECH 2023 Forum, National Harbor, MD, USA, 23–27 January 2023. [CrossRef]
22. Lu, X.; Huang, J.; Song, L.; Li, J. An improved geometric parameter airfoil parameterization method. *Aerosp. Sci. Technol.* **2018**, *78*, 241–247. [CrossRef]
23. Drexler, C. Design by Optimization of a Multi-Element Airfoil for Drag Power Kite. Master's Thesis, Technische Universität München, Munich, Germany, 2019.
24. Hansen, N. The CMA Evolution Strategy: A Tutorial. *arXiv* **2016**, arXiv:1604.00772. https://doi.org/10.48550/ARXIV.1604.00772.
25. De Fezza, G.; Barber, S. Parameter analysis of a multi-element airfoil for application to airborne wind energy. *Wind Energy Sci.* **2022**, *7*, 1627–1640. [CrossRef]
26. Benini, E.; Ponza, R.; Massaro, A. High-lift multi-element airfoil shape and setting optimization using multi-objective evolutionary algorithms. *J. Aircr.* **2011**, *48*, 683–696. [CrossRef]

27. Ragheb, A.; Selig, M. Multi-element airfoil configurations for wind turbines. AIAA 2011-3971. In Proceedings of the 29th AIAA Applied Aerodynamics Conference, Honolulu, HI, USA, 27–30 June 2011. [CrossRef]
28. Florjancic, D. Improved Design of a High Lift System for General Aviation Aircraft. Master's Thesis, Delft University of Technology, Delft, The Netherlands, 2015. Available online: http://resolver.tudelft.nl/uuid:a0bcdbba-3ccc-4622-ab8d-6ac2e4a1e598 (accessed on 25 September 2022).
29. Luchsinger, R.H. Pumping Cycle Kite Power. In *Airborne Wind Energy*; Ahrens, U., Diehl, M., Schmehl, R., Eds.; Green Energy and Technology; Springer: Berlin/Heidelberg, Germany, 2013; Chapter 3, pp. 47–64. [CrossRef]
30. Yu, X.; Gen, M. *Introduction to Evolutionary Algorithms*; Springer: London, UK, 2010. [CrossRef]
31. Slowik, A.; Kwasnicka, H. Evolutionary algorithms and their applications to engineering problems. *Neural Comput. Appl.* **2020**, *32*, 12363–12379. [CrossRef]
32. Mathworks. What Is the Genetic Algorithm? Available online: https://www.mathworks.com/help/gads/what-is-the-genetic-algorithm.html (accessed on 31 January 2023).
33. Deb, K.; Agrawal, S.; Pratap, A.; Meyarivan, T. A fast elitist non-dominated sorting genetic algorithm for multi-objective optimization: NSGA-II. In *Parallel Problem Solving from Nature PPSN VI. PPSN 2000. Lecture Notes in Computer Science, vol 1917*; Schoenauer, M., Deb, K., Rudolph, G., Yao, X., Lutton, E., Merelo, J.J., Schwefel, H.P., Eds.; Springer: Berlin/Heidelberg, Germany, 2000; pp. 849–858. [CrossRef]
34. Deb, K. Multi-objective optimisation using evolutionary algorithms: An introduction. In *Multi-Objective Evolutionary Optimisation for Product Design and Manufacturing*; Wang, L., Ng, A.H.C., Deb, K., Eds.; Springer: London, UK, 2011; pp. 3–34. [CrossRef]
35. Mathworks. Gamultiobj—Find Pareto Front of Multiple Fitness Functions Using Genetic Algorithm. Available online: https://www.mathworks.com/help/gads/gamultiobj.html (accessed on 31 January 2023).
36. Peerlings, B. *A Review of Aerodynamic flow Models, Solution Methods and Solvers and Their Applicability to Aircraft Conceptual Design*; Literature study report; Delft University of Technology: Delft, The Netherlands, 2018. Available online: http://resolver.tudelft.nl/uuid:d14b5f60-7000-439b-8785-62e513902bf8 (accessed on 20 September 2022).
37. Hölling, M.; Peinke, J.; Ivanell, S. (Eds.) *Wind Energy-Impact of Turbulence*; Research Topics in Wind Energy; Springer: Berlin/Heidelberg, Germany, 2014; Volume 2. [CrossRef]
38. Omar, E.; Zierten, T.; Hahn, M.; Szpiro, E.; Mahal, A. *Two-Dimensional Wind-Tunnel Tests of a NASA Supercritical Airfoil with Various High-Lift Systems. Volume 2: Test Data*; Technical Report NASA CR-2215; NASA: Washington, DC, USA, 1977.
39. Anderson, J. *Introduction to Flight*, 8th ed.; McGraw Hill Education: New York, NY, USA, 2016.
40. Menter, F. Zonal two equation kw turbulence models for aerodynamic flows. AIAA-93-2906. In Proceedings of the 23rd Fluid Dynamics, Plasmadynamics, and Lasers Conference, Orlando, FL, USA, 6–9 July 1993. [CrossRef]
41. Folkersma, M.; Schmehl, R.; Viré, A. Boundary layer transition modeling on leading edge inflatable kite airfoils. *Wind Energy* **2019**, *22*, 908–921. [CrossRef] [PubMed]
42. Abbott, I.H.; Doenhof, A.E.V. *Theory of Wing Sections*; Dover Publications: New York, NY, USA, 1960.
43. Syms, G.F. Analysis of general-aviation aircraft wing sections with drooped leading edges. *J. Aircr.* **2006**, *43*, 1029–1035. [CrossRef]